SUBMISSION TO GEOTECHNICAL TESTING JOURNAL

DATE:

27/03/2019

TITLE:

Apparatus for measuring pipe-soil interaction behaviour using shallow 'pipe-like' penetrometers

AUTHORS:

Schneider, M.A.[1], Stanier, S.A.[2], White, D.J.[3] and Randolph, M.F.[4]

POSITIONS AND AFFILIATIONS:

[1] Research Student at the Centre for Offshore Foundation Systems, University of Western Australia

[2] University Senior Lecturer, University of Cambridge (formerly University of Western Australia)

[3] Professor, University of Southampton (formerly University of Western Australia)

[4] Professor at the Centre for Offshore Foundation Systems, University of Western Australia

CONTACT ADDRESS:

Dr Sam Stanier
Cambridge University Engineering Department
Trumpington Street
Cambridge
CB2 1PZ
United Kingdom

NUMBER OF WORDS, FIGURES AND TABLES:

Words: ~4800
Figures: 13
Tables: 1

KEYWORDS:

Shallow penetrometer; hemiball; toroid; offshore engineering; in-situ testing; pipe-soil interaction

APPARATUS FOR MEASURING PIPE-SOIL INTERACTION BEHAVIOUR USING SHALLOW 'PIPE-LIKE' PENETROMETERS

Schneider, M.A., Stanier, S.A., White, D.J. and Randolph, M.F.

ABSTRACT

Reliable characterisation of surficial marine sediments is essential to ensure safe and economical design of subsea infrastructure for offshore energy facilities (e.g. seabed cables, pipelines and shallow foundations). Conventional in-situ testing methods (e.g. CPT or T-Bar) require careful interpretation to account for the effects of shallow embedment, while laboratory tests are affected by sampling induced disturbances, the impact of which can be significant at the low stress levels relevant to the design of subsea infrastructure. This paper describes two novel box-core sized shallow penetrometers – the hemiball and toroid – which mimic the shape of subsea pipelines and have been designed to reliably measure the strength, consolidation and frictional properties of surficial offshore sediments. The development and specification of the actuator used to operate these probes, is also described. Another major benefit of these penetrometers, which are intended to be used offshore for on-deck testing aboard a survey vessel, is their capability to generate effective stress interpretations of the soil behaviour, since pore pressures transducers are installed and monitored throughout testing. The results of a first laboratory proof test are presented to illustrate the potential of this novel sensor concept.

INTRODUCTION

Reliable characterisation of surficial marine sediments in deep water is becoming increasingly important as the demand for subsea infrastructure increases. Seabed cables, pipelines and shallow foundations are three examples of subsea infrastructure that are founded at shallow depths in very soft offshore soils (s_u < 10 kPa). It is difficult to assess the strength of such surficial sediments with conventional testing tools (e.g. CPT or T-Bar), due (i) to the low strengths and (ii) the requirement for adjustment of the measurements to account for shallow embedment (White et al., 2010).

Routine laboratory tests (e.g. simple shear or triaxial tests) performed on recovered tube samples may be adversely affected by sampling-induced disturbances (Clayton et al., 1998; Hover et al., 2013) and therefore also yield unreliable test results. Similarly, performing direct shear or interface shear tests at low stress levels (σ'_n < 20 kPa) is challenging, with the measurements often requiring significant 'system friction' corrections dependent on the design of the apparatus (Lehane & Liu, 2013), which adds uncertainty to the interpretation. Other more exotic laboratory tests, such as the tilt table (Pedersen et al., 2003) and Cam-Tor apparatus (Kuo et al., 2015) have been developed that are better suited to testing soil at low stress levels. However, both require samples to be recovered to an onshore laboratory, which creates a delay after sampling before the soil properties are determined and leaves the samples open to potential disturbances in transit.

The Fugro SMARTPIPE (Hill & Jacob, 2008; White et al., 2010) is a 200 mm diameter model pipeline equipped with surface pore pressure transducers and controlled in-situ on the seabed by a three degree of freedom hydraulic actuator (controlling axial, lateral and settlement movements). The device can perhaps be regarded as the 'gold standard' tool for making pipe-soil interaction measurements. However, its application is costly due to the timescales required for testing on soft clay seabeds, mainly because of the low values of the coefficient of consolidation (c_v) expected and the relatively large diameter of the model pipeline.

A potential alternative is to perform in-situ measurements using shallow penetrometers, such as the hemiball or toroid (Figure 1), that mimic (in cross section) the shape of subsea infrastructure such as pipelines. Prototypes of these devices were developed as part of the activities of the Remote Intelligent Geotechnical Seabed Surveys Joint Industry Project (RIGSS JIP) as summaraised in White et al. (2017). In principle these devices facilitate more reliable measurement of near-surface soil properties (Yan et al., 2011; Stanier & White, 2014). Both probes are envisaged to be capable of measuring all of the essential pipe-soil interaction parameters required in modern geotechnical pipeline (or seabed cable) design, in just a couple of relatively short tests (~30 mins each) performed in a box core sample (~0.5 m by ~0.5 m by ~0.5 m in volume) recovered to the deck of a survey vessel.

A shallow penetrometer test consists of three stages: penetration, dissipation and rotation, and interpretation of the data captured in these stages yields parameters quantifying, respectively, the undrained strength, consolidation and friction characteristics of soft near-surface sediments. Interpretation methods already exist for both the toroid and hemiball. For interpretation of the penetration stage, Stanier & White (2014) reported outcomes from a large deformation finite element parametric study of the undrained penetration stage (LDFE), using the RITSS methodology (remeshing and interpolation technique with small strains) of Hu & Randolph (1998) in combination with the Tresca constitutive model. Yan et al. (2017) provided models to interpret the dissipation and rotation stages. The latter solutions were developed from wished-in-place small-strain finite element simulations incorporating the Modified Cam Clay (MCC) soil model, which is appropriate for the fine-grained normally consolidated conditions prevalent in the subsea environment where shallow penetrometer tests would be applicable.

This paper describes the apparatus required to execute shallow penetrometer tests offshore, within a box core sample recovered to the deck of a survey vessel. We demonstrate that careful consideration must be given to: (i) the design of the actuator; and (ii) the specification of the sensors incorporated in the shallow penetrometers, to ensure accurate resolution of the

measurements. An example test on a soft kaolin clay sample is used to illustrate the capabilities of the system.

SHALLOW PENETROMETERS

Design and size

The toroid and hemiball penetrometers are pipe-like devices (in cross-section) that closely mimic the infrastructure being investigated. Consequently, the uncertainty resulting from geometric conversion of the interface response to that representative of a pipeline or subsea cable is minimised. Figure 2 presents detailed engineering drawings of the penetrometer designs for the box core sized hemiball (100 mm diameter, D) and toroid (25 mm diameter, D; 50 mm lever arm, L; and aspect ratio, L/D = 2 after Yan, 2011).

The size of the shallow penetrometers was selected to balance two opposing drivers: on one hand the devices should ideally be similar in size to typical subsea pipelines to minimise scaling uncertainty, whilst on the other hand the devices ought to be small enough in cross-sectional diameter such that the dissipation characteristics and evolving soil response can be measured in a practical timescale within a box core sample (typically: 0.5 m x 0.5 m). The device should also be large enough that small undulations of the soil surface do not cause the penetration to be excessively non-uniform around the circumference of the device, hampering interpretation.

Pore pressure transducers are located at various positions around the probe, therefore facilitating an effective stress interpretation of the frictional response of the soil-penetrometer interface. For the hemiball a total of 5 pore pressure transducers are positioned on the penetrometer interface (Figure 1), with two transducers at the so-called midface (abbr. *mf*, at an angle of 45 degrees) and intermediate positions (abbr. *int*, at an angle of 22.5 degrees) and one at the invert (or tip) of the device. On the toroid all four pore pressure sensors are located at the invert (abbr. *inv*). The shallow penetrometers attach to an actuator using an M10 threaded

connector and locking collar. The interior of the shallow penetrometers was hollowed out for placement of pore pressure transducers within the cavity of the device.

Interface finish

In order for the shallow penetrometers to be able to measure the drained friction angle during slow sustained rotation, the penetrometer surface must be sufficiently rough. To identify a suitable surface finish, low stress drained interface shear box tests (σ'_n ~8-12 kPa; 82 mm diameter interface; see also Boukpeti & White, 2017) were conducted on normally consolidated kaolin clay using machined and shot-blasted plastic inserts (Polyoxymethylene).

At such low stress levels, it is important to account for the weight of the upper half of the shear box, hence the corrections proposed by Lehane & Liu (2013) were incorporated into the interpretation of the interface shear box data. Two different correction procedures were considered, depending on whether or not soil was squeezed into the gap between the two halves of the direct shear apparatus (approach 1: no soil squeezed between upper and lower shear box; and approach 2: soil present between shear boxes). Nevertheless, for the purposes of identifying the degree of interface roughness, both interpretation methods result in an identical normalised response (normalisation: $\tan\delta/\tan\phi'$).

Figure 3 shows the results of an example interface shear box test at an effective normal stress of about ~10.7 kPa, normalised by the drained friction coefficient, $\tan\phi'$, interpreted from complimentary direct shear tests performed on the same material. The machined inserts mobilise around 75% of the drained friction angle, whereas the shot-blasted finish mobilised the full drained friction angle.

INSTRUMENTATION

Load cell

Penetration resistance: The shallow penetrometer penetration resistance model of Stanier & White (2014) – which is based on an extensive large deformation finite element parametric study using the Tresca soil model – was used to estimate the vertical load required to penetrate the box core sized shallow penetrometers into soil with a range of undrained strength profiles. The undrained penetration resistance, V, for a shallow penetrometer consists of two different components: (i) the geotechnical resistance, V_{geot}; and (ii) the soil buoyancy, V_b, according to:

$$V = V_{geot} + V_b = N_{c,nom}\, A_{nom}\, s_{u0} + f_b\, V_s\, \gamma' \tag{1}$$

The geotechnical resistance is generated by the soil strength itself, here represented by s_{u0}, which describes the intact strength at the invert level of the probe. A_{nom}, representing the nominal area, can be calculated as:

$$A_{nom,Hemi} = \pi D^2/4 \qquad or \qquad A_{nom,Toro} = 2\pi L D \tag{2}$$

The bearing capacity factor, $N_{c,nom}$, varies as a function of the embedment depth, w, and the average dimensionless undrained shear strength, $k_{su} D/s_{u,avg}$ (Stanier & White, 2014). The soil buoyancy felt by the probe is a function of the effective unit soil weight, γ', the submerged penetrometer volume below the original mudline, V_s, and an enhancement factor, f_b, to account for the increase in soil buoyancy in excess of that due to the nominal embedment depth below the soil surface, due to soil heave around the periphery of the penetrometer.

Torsional resistance: For normally consolidated or lightly over-consolidated sediments typically found offshore, the peak torsional resistance at the interface of a toroidal or hemispherical penetrometer is limited by the consolidated undrained (CU – for rapid tests) or

drained (D – for slow tests) behaviour of the soil. For the case of zero excess pore pressure, the (drained) torsional resistance, T, of the soil is:

$$T_{Hemi} = \tan\delta\, \zeta_{Hemi}\, V\, r_{eff} \qquad or \qquad T_{Toro} = \tan\delta\, \zeta_{Toro}\, V\, L \tag{3}$$

with a limiting value for a fully rough interface obtained assuming $\tan\delta = \tan\phi'$. The parameter ζ is a wedging factor to account for the non-planar surface of the shallow penetrometers and depends on the semi-angle, $\theta = cos^{-1}(1\text{-}2w/D)$, of the embedded segment. Following Yan (2014) for the hemiball and White & Randolph (2007) for the toroid this factor may be expressed as:

$$\zeta_{Hemi} = \frac{3\sin^2\theta}{2\left(1-\cos^3\theta\right)} \le 1.5 \qquad or \qquad \zeta_{Toro} = \frac{2\sin\theta}{\theta + \sin\theta\,\cos\theta} \le 1.27 \tag{4}$$

The effective radius is required to convert the measured torque into an equivalent axial force for a pipeline. For the hemiball r_{eff} can be expressed as a function of the semi-angle, θ, as:

$$r_{eff} = \frac{D\,\sin\theta}{3} \tag{5}$$

whereas for the toroid it is equal to the lever arm of the device, which is 50 mm.

Sensor selection: Figure 4 presents the vertical force required to penetrate a fully rough hemiball or toroid penetrometer to a normalised depth of w/D = 0.5 as well as the torque necessary to rotate the device under drained conditions (i.e. no excess pore pressure generation). Undrained shear strength profiles with different mudline strengths s_{um} (0-8 kPa) and gradients with depth k_{su} (8-0 kPa/m) are considered for the vertical load estimates in Figure 4a and interface friction angles corresponding to 20˚ and 40˚ for the torque estimates in Figure 4b. Due to the shallow probe embedment, w, it turns out that the vertical penetration resistance, V, is largely independent on the combination of s_{um} and k_{su}, thus essentially proportional to the

undrained strength at the device invert, $s_{u0} = s_{um}+0.5Dk_{su}$ for $w/D = 0.5$, as shown in Figure 4a. The dashed lines represent the load and torque generated during vertical penetration and rotation, respectively, with an effective normal stress, σ'_n, of 20 kPa acting on the surface of the penetrometer, which is a realistic upper limit of the operative stress that pipelines and shallow foundation apply to the seabed. Based on these specifications a Futek MBA500 combined vertical load and torque cell (model number: FSH00747; load capacity: 444 N; torque capacity: 11.3 Nm; safe overload: 150%; temperature compensation range: 15-70˚) was selected. This sensor has sufficient capacity to allow testing to embedments greater than 0.5*D*, as pipelines have been known to embed by more than one diameter in softer seabed sediments (Westgate et al. 2012).

Pore pressure transducers

Excess pore pressure: The maximum excess pore pressure is expected to be recorded towards the end of the undrained penetration stage and the beginning of the consolidation phase. A simple approximation of the maximum required sensor capacity can be made by assuming that the maximum average excess pore water pressure $\Delta u_{ave,max}$ is equivalent to the total contact stress, σ_n, according to:

$$\Delta u_{ave,\max} \approx \sigma_n = \frac{N}{A_c} = \frac{\zeta V}{A_c} \tag{6}$$

where

$$A_{c,Hemi} = \pi\left[\left(\frac{\sin\theta D}{2}\right)^2 + w^2\right] \qquad or \qquad A_{c,Toro} = 2\pi D L \cos^{-1}\left(\frac{D-2w}{D}\right) \tag{7}$$

Figure 5 shows that for a penetration depth of 0.5*D* (i.e. full embedment) the maximum average excess pore water pressure is ~45 kPa, assuming the same soil profiles as for the previous load

cell calculations (penetration resistance). A Honeywell 26PC series sensor (model number: 26PCCFA6G; differential pressure capacity: 100 kPa; temperature compensation range: 15-70˚) was selected. As for the selected load cell, this pore pressure sensor has a reserve of capacity.

Plastic filters were manufactured from a 35μm porous hydrophilic polyethylene sheet to provide a porous barrier between the sensing element of the transducers and the soil particles. Three different backfilling liquids – used to saturate the void within and behind the plastic filters – were tested in the laboratory, including silicone oil, glycerin and de-aired water. The most consistent pore pressure readings were achieved with de-aired water, as the other two liquids appeared to react with the clay particles leading to coagulation of lumps of viscous material that eventually clogged the filters during testing, leading to drift in excess pore pressure dissipation measurements.

Calibration of instrumentation

To calibrate the two channels of the load cells (vertical force and torque) built into the shallow penetrometers, a calibration frame was developed that could load the penetrometer with vertical force and torque in isolation or simultaneously. This allowed the potential for any cross-interference of the measurements (e.g. adverse effect of force measurements on recorded torque) to be checked. The pore pressure transducers were calibrated by comparing the output voltages of each sensor to the pressure measured by a calibrated reference sensor.

ACTUATOR DESIGN

An actuator with two degrees of freedom (vertical displacement and rotation), which can be mounted on a strongbox in the laboratory, or a box core sleeve in the field, is required to operate the shallow penetrometers.

Figure 6 shows the final design of such an actuator, which was built from predominantly off-the-shelf components. It consists of a linear actuator (Parker Hannifin; model number: 404300XRMP; range: 300 mm; maximum vertical load: 900 N; maximum torque: 45 Nm; backlash: ±1.3 μm), with the vertical and rotational axes driven by AC servomotors (Parker Hannifin; model number: SM162BE-NFLN; maximum rpm: 4000; peak torque) and Parker Hannifin amplifiers (model number: VIX500).

Gearboxes are required to achieve appropriate penetration and rotation rates. It is critical that these have minimal backlash to: (i) ensure accurate load control on the vertical axis; and (ii) allow robust dimensionless interpretations of the time required to transition from undrained to drained sliding behaviour. For example, on the rotational axis, modest backlash of up to 3° can be shown to result in an uncertainty of almost one order of magnitude in the determination of the dimensionless time ($T_{rot} = c_v\, t / D^2$). Depending on where the gearbox is within its range of backlash, there will be a varying amount of rotation of the motor prior to the shallow penetrometer beginning to rotate. This can have a profound effect on the interpretation of the measurements, so it is critical that high quality gearboxes with minimal backlash are used. Consequently, both axes were geared down using Harmonic Drive gearboxes (model number: CSF-14-100-1U-CC-F-1; reduction ratio 100:1), which make use of the strain-wave principle to achieve the drive speed reduction in a compact form factor with minimal backlash (0.025° per unit). This backlash corresponds to a rotational displacement at the effective radius of the toroid (r_{eff} = 50 mm $\forall$ w/D) and hemiball (r_{eff} = 33.33 mm at an embedment w/D = 0.5) of

~43.6 and ~29.1 μm, respectively. For the vertical axis, the gearbox and linear actuator backlash combined correspond to ~1.65 μm of vertical movement.

Drive speed requirements

The actuator has been designed to be able to perform miniature probe tests (T-bar, ball and cone penetrometer) as well as shallow penetrometer tests. The vertical penetration speed required, $v_{pen,ud}$, was determined by setting $v_{pen}\ D\ /\ c_v$ equal to 100, which ensures undrained penetration conditions for a pipeline (Chatterjee et al. 2013). Similarly, the required axial sliding velocity was identified by setting the dimensionless velocity term $V_{rot} = v_{rot}D/c_v$ equal to 10, which is sufficient to ensure undrained conditions for axial sliding of a seabed pipeline according to Randolph et al. (2012). A non-dimensional velocity of V_{rot} = ~10 corresponds to a dimensionless time of $T_{rot} = c_v t/D^2$ ~0.002, given a normalised displacement to failure of around ~0.02 (Figure 13b), which is consistent with numerical calculations published by Yan et al. (2014). The corresponding angular velocity, which can be expressed as a function of the rotation speed at a distance equal to the effective radius, $v_{rot,eff}$, was then calculated as follows:

$$\omega\ (^\circ / s) = \frac{v_{rot,eff}}{r_{eff}}\left(\frac{180}{\pi}\right) = \frac{c_v V_{rot}}{D r_{eff}}\left(\frac{180}{\pi}\right) \tag{8}$$

Actuator speed requirements for the vertical and rotational axes were determined for undrained penetration and rotation conditions assuming c_v in the range of 0.1-100 m^2/yr and motor rotational speed in the range of 1-4000 rpm. Figure 7 shows that for the vertical axis a single 100:1 reduction drive is sufficient to conduct undrained tests with both the shallow penetrometers and miniature probes for a wide range of c_v. For the rotational axis a pair of 100:1 reduction drives, giving a total reduction of 10,000:1, is required to achieve undrained rotation for the same range of c_v for the box core sized shallow penetrometers described in this paper (Figure 7b).

MOTION CONTROL & DATA ACQUISITION

Reliable real-time data feedback from the bi-axial load cell is crucial in order to run tests in both displacement- and load-controlled modes. A BNC-cable serves as load-feedback transfer from the moving probe to the stationary motion control system. The system is driven by custom control software, which is based on the PACS-software (De Catania et al., 2010) and specifically modified for box-core penetrometer use. The in-house developed control software allows penetrometer tests to be fully automated by either running positional or load-controlled sequences, so-called waveforms. Before being able to properly test the novel probes, though, it was important to evaluate the correct PID-setting to cope with the low stresses expected in these tests, and to cope with any potential vessel motion during offshore deployment.

Live data (load, torque and pore pressures) is continuously streamed through a custom-built wireless DAQ system, that is capable of transmitting data on eight different channels using a Wi-Fi link (Figure 8a), minimising the number of cables required to bridge the gap between the rotating (device) and non-rotating (actuator) assemblies. A LabVIEW based DigiDAQ software, which was also created in-house at COFS (Gaudin et al., 2009), is used to process and display the measurements onscreen in real-time (Figure 8b).

BASIC TEST PROTOCOL

A basic shallow penetrometer test typically consists of four testing stages: the penetration, dissipation and rotation stages followed by a further penetration / extraction stage. Several near-surface soil properties can be inferred directly from measurements of the penetration resistance, V, the mobilised torque, T, the pore water pressure, u, as well as the embedment depth, w. The key measurements captured and the parameters that can be interpreted from them are summarized in Table 1.

Table 1: Main testing stages and soil properties of interests

Testing stage		Key measurements	Targeted properties
1	Penetration	V, w	s_u
2	Dissipation	$u(t)$	c_v
3	Rotation	T, u, w	τ_u , δ, ϕ', (κ/λ) *
4	Penetration & Extraction	V, w	$s_{u,c}$

* Different properties can be determined depending on rotation speed and interface roughness

Penetration stage: The probe is penetrated vertically into the soil at an approximately undrained rate, defined as:

$$V_{pen} = \frac{v_{pen} D}{c_v} \geq 100 \tag{9}$$

Because the diameter of the hemiball is greater than that of the toroid a slower penetration speed v_{pen} can be used for the hemiball, whilst maintaining undrained conditions. The maximum target load resulting in an appropriate average effective normal stress on the surface of the probe is set prior to penetration (typically such that σ'_n is in the range of 5-20 kPa). The device is then penetrated into the soil until that target load is reached, or the indicated embedment of the device is equal to a maximum embedment depth (typically set as 0.3D).

Dissipation stage: The penetration induced excess pore pressure dissipation is monitored whilst maintaining the vertical load applied to the shallow penetrometer, therefore mimicking the self-weight of a pipeline or shallow foundation. As for standard practice for CPTu measurements, in order to estimate c_v accurately from the measured excess pore pressure response, $u(t)$, at least ~50% of the initial excess pore pressures should be allowed to dissipate. Ideally, for fully consolidated conditions to be measured during the rotation phase, >> 90% of the excess pore pressures would need to be allowed to dissipate.

Rotation stage: Following dissipation, the shallow penetrometer is rotated about its axis whilst continuing to maintain the vertical load applied to the penetrometer. Depending on the rate and duration of the rotation, as well as the soil consolidation coefficient, the undrained interface friction τ_u and the drained interface friction angle δ can be evaluated. To estimate the fully drained interface resistance the rotation needs to be conducted for a sufficiently long period of time (i.e. dimensionless time $T_{rot} = c_v\, t / D^2 \geq 1$; after Randolph et al., 2012; Yan et al., 2014), so that >> 90% of excess pore water pressures can dissipate. Test durations are on the order of an hour but depend on the coefficient of consolidation, c_v, and device diameter, D. The interface shear box test data presented earlier shows that if the surface of the shallow penetrometer is sufficiently rough the internal friction angle of the soil, ϕ', can be determined directly from the torque measurements.

As a variation of the rotation phase a sequence of several fast rotation cycles with intervening dissipation periods can also be conducted. This models the response of a pipeline being subjected to heating and cooling cycles (and associated expansion and contraction in length) such as occur during the transition between operation and shutdown periods. Numerical simulation of this process (Yan et al., 2014) shows that this variation of test can yield additional information regarding the rate (with cycles) at which hardening occurs, which depends on the ratio of κ/λ.

Further penetration & extraction: Following rotation, the shallow penetrometer can be penetrated further into the soil before finally extracting it, allowing the consolidated undrained strength, $s_{u,c}$, to be estimated.

Basic penetrometer test: Figure 9 illustrates schematically the stages described above when combined as a 'basic' shallow penetrometer test in terms of the expected accumulated displacement and applied rotation. The rotation stage is subdivided into three stages with reducing rotation speed. This allows the 'backbone curve' (Randolph et al. 2012) – which

describes the transition from undrained to drained sliding for a pipeline in non-dimensional terms – to be measured in a single test. The initial rotation is performed sufficiently fast that the full sliding resistance is mobilised prior to any effect of drainage, meaning that the fully undrained interface strength is measured. The subsequent reductions in rotation rate are required to limit the settlement of the shallow penetrometer as sustained fast undrained rotation leads to excessive settlement in soft clay samples.

EXAMPLE APPLICATION

A large strongbox of kaolin clay (1300 mm by 390 mm in plan) was preconsolidated under a constant surcharge of 20 kPa, creating a soft and broadly homogeneous sample with strength of ~2 kPa. There is a slight tendency for the strength to reduce with depth, which is caused by frictional losses along the vertical sidewalls of the strongbox during consolidation. Example time histories for the applied vertical load, rotation angle, measured torque and average excess pore pressures are shown in Figure 10. Results of the penetration, dissipation and rotation stages of a 'basic test' conducted using the toroid penetrometer are presented in Figure 11, Figure 12 and Figure 13, respectively. This data demonstrates that: (i) the load control managed to maintain the vertical load applied to the toroid within ± ~1 N of the target load; and (ii) that the dissipation characteristics of the soil can be measured very accurately and reasonably using the pore pressure sensors installed in the device.

The model proposed by Stanier & White (2014) was used to back-analyse the penetration stage (penetration to w/D = 0.3 at an undrained rate) and estimate the undrained soil strength profile of the sample. Three interpreted toroid tests are shown in Figure 11, alongside a (5 mm diameter) T-bar test to provide context, both with and without shallow embedment correction after White et al. (2010). The shallow penetrometer tests produce very consistent strength predictions that fall between the corrected and uncorrected T-bar interpretations, which assumed an intermediate roughness T-bar factor, $N_{T\text{-}bar}$, equal to 10.5.

Existing small strain finite element solutions (Yan et al., 2017) were used to back-analyse the pore pressure dissipation and determine the coefficients of consolidation, c_v. The raw measurements were adjusted following Sully et al. (1999), before being normalised by the initial excess pore pressure at the onset of dissipation. The resulting normalised dissipation is then plotted against the non-dimensional dissipation time, $T_{dis} = c_v\, t \,/\, D^2$, in semi-logarithmic space (Figure 12a) allowing the c_v assumed in the normalisation of the excess pore pressure measurements to be adjusted until the experimental measurements coincide with the finite element solution at $\Delta u/\Delta u_i = 0.5$ (i.e. ~50% of the excess pore pressure had dissipated). The three tests presented in Figure 12 show excellent repeatability with estimated c_v-values of 4.3, 4.6 and 5.0 m^2/yr. The stated values correspond to the invert level of the probe and are again consistent with other independent measurements for kaolin clay, as shown in Figure 12b.

Figure 13 shows the back-analysis of the rotation stage with (a, b) total and (c) effective stress interpretations, with each rate (fast, medium and slow) represented by a different color. Observations made during the test indicated that the actuator settlement overestimated the contacting surface area of the device due to radial heave of soil at the periphery of the device. Consequently, the semi-angle of the embedded section of the device was capped at $\pi/4$, which was estimated to be an appropriate value based on photographic evidence recorded during the test.

Total stress interpretation: Figure 13a shows an excellent match between the experimental and the theoretical backbone curve derived numerically (SSFE). The normalised axial friction starts at a value of about ~0.24, which, after reducing the total penetrometer friction factor to account for wedging ($\zeta \approx 1.1$), results in an undrained stress ratio $(s_u/\sigma'_v)_{nc}$ of ~0.215. This value is slightly higher than typical for UWA kaolin clay (Hu et al., 2014; Lee et al., 2013), which could be a result of the soil beneath the penetrometer remaining partially over-consolidated during the rotation phase. After dissipation of the excess pore pressures a plateau in normalised friction of roughly ~0.36 is reached, representing the drained penetrometer friction. Again after

accounting for wedging, the equivalent drained interface friction angle is ~18-19°, which is close to the friction angle determined in the interface shear box tests (approach 2: ϕ' = ~19-20.5°) and in good agreement with the measurements of, for example, Chen & Randolph (2007).

Effective stress interpretation: The average effective normal stress $\sigma'_{n,ave}$ and shear stress τ_{ave} were evaluated as:

$$\sigma'_{n,ave} = \sigma_n - \Delta u_{ave} = \frac{\zeta V}{A_c} - \beta \Delta u_{inv} \qquad and \qquad \tau_{ave} = \frac{(T / r_{eff})}{A_c} \tag{10}$$

where the average excess pore pressure Δu_{ave} acting at the probe interface has been approximated by multiplying the invert measurement Δu_{inv} (or the mean of several invert measurements) by a scaling factor β. This is generally less than unity, acknowledging that the invert measurement of excess pore pressure will tend to overestimate the average excess pore pressure acting on the interface of the device.

Coupled numerical simulations performed by Yan (2014) indicated that the appropriate value for β is in the range of 0.65 to 0.80. A value of 0.725, which corresponds to the mean of the given range, was used for all calculations. The measured excess pore pressures were corrected according to Sully et al. (1999) to account for the slight lag in measured dissipation response observed during the fast rotation phase.

Figure 13c illustrates the increase in effective stresses and accordingly the interface friction, as the excess pore water pressures gradually dissipate over time. Two effective stress envelopes generated from the shear box tests bracket the toroid measurements. The two interpretations of the interface shear box tests are for two of the correction scenarios identified by Lehane & Liu (2013): (i) where the load applied to the sample interface is reduced to some degree due to friction generated between the soil and the vertical sidewalls of the upper half of the shear box;

and (ii) where the load applied to the sample interface is increased due to soil squeezing into the gap and mobilising the residual friction of the soil between the two halves of the shear box. The lower limit corresponds to the latter approach, which seems more suitable here, as post-test inspections revealed the presence of kaolin clay between the upper and lower halves of the shear box.

The value of the shallow penetrometer is that the whole spectrum of behaviour – undrained to drained – is explored in a single test that encompasses a range of effective normal stress levels. In contrast the interface shear box data comprises several drained tests performed at discrete effective normal stress levels, which are more time consuming to perform and more sensitive to assumptions in the interpretation.

CONCLUSIONS

This paper has described apparatus and testing techniques for pipe-shaped toroidal and hemispherical shallow penetrometers. These devices are capable of reliably inferring undrained strength, consolidation and friction characteristics of surficial offshore soil. A box-core scale version of each device has been developed for use offshore on a survey vessel and design considerations with respect to actuation, instrumentation, data acquisition and interpretation have been described. Finally, a proof of concept toroid test was used to highlight the potential of shallow penetrometers in rapidly defining pipe-soil interaction parameters. The measurements derived with the toroid compare favorably with data from conventional miniature probes such as the T-bar (for undrained strength measurement during penetration) and interface shear box tests (for axial friction measurement during rotation) performed on the same soil, but have the advantage of being quicker to perform and less sensitive to interpretation assumptions.

ACKNOWLEDGEMENTS

The research presented here forms part of the activities of the Centre for Offshore Foundation Systems (COFS), currently supported as a node of the Australian Research Council Centre of Excellence for Geotechnical Science and Engineering. The first author is grateful for the support provided by an International Postgraduate Research Scholarship (IPRS) from the Australian Government. The second author is the holder of an ARC DECRA Fellowship (DE170100119). This work has been further supported by Shell, via the Shell EMI Chair in Offshore Engineering held by the third author, and by Fugro via the Fugro Chair in Geotechnics held by the fourth author.

NOTATION

A_c	surface contact area
A_{nom}	nominal area
c_v	coefficient of consolidation
D	device diameter
dx	horizontal displacement (shear box)
f_b	soil buoyancy factor
k_{su}	gradient of undrained strength profile
L	lever arm (toroid penetrometer)
N	total normal load
$N_{c,nom}$	bearing capacity factor
r_{eff}	effective radius
s_u	undrained shear strength
s_{u0}	undrained shear strength at penetrometer invert
$s_{u,avg}$	average undrained shear strength
$s_{u,c}$	consolidated undrained shear strength
s_{um}	undrained shear strength at mudline
T	mobilised torque
T_{dis}	dimensionless time (dissipation stage)
T_{rot}	dimensionless time (rotation stage)
t	time
u	pore water pressure
V	vertical penetration resistance
V_b	resistance due to soil buoyancy
V_{geot}	geotechnical resistance
V_{pen}	dimensionless velocity (penetration stage)
V_{rot}	dimensionless velocity (rotation stage)
V_s	submerged penetrometer volume
v_{pen}	vertical penetration speed
$v_{pen,ud}$	vertical penetration speed (undrained rate)
v_{rot}	velocity during rotation stage
$v_{rot,eff}$	velocity during rotation stage at effective radius r_{eff}
w	embedment depth

α	rotation angle
β	scale factor regarding excess pore pressure
γ'	effective unit weight
Δu	excess pore water pressure
Δu_{ave}	average excess pore water pressure
Δu_i	initial excess pore water pressure at consolidation start
Δu_{inv}	excess pore water pressure at probe invert
δ	drained interface friction angle
ζ	wedging factor
θ	semi-angle of embedded segment
κ	slope of elastic compression line

λ	slope of virgin compression line
σ_n	total normal contact stress
σ'_n	effective normal contact stress
$\sigma'_{n,ave}$	averaged effective normal stress at probe interface
τ_{ave}	average shear stress at probe interface
τ_u	undrained interface friction
ϕ'	effective angle of internal friction
ω	angular velocity

REFERENCES

Boukpeti, N. & White, D. J. (2017). Interface shear box tests for assessing axial pipe-soil resistance. *Géotechnique* **67**, No. 1, 18-30.

Chatterjee, S., White, D. J. & Randolph, M. F. (2013). Coupled consolidation analysis of pipe–soil interactions. *Canadian Geotechnical Journal* **50**, No. 6, 609-619.

Chen, W. & Randolph, M. F. (2007). External radial stress changes and axial capacity for suction caissons in soft clay. *Géotechnique* **57**, No. 6, 499-511.

Chow, S. H., O'loughlin, C. D. & Randolph, M. F. (2014). Soil strength estimation and pore pressure dissipation for free-fall piezocone in soft clay. *Géotechnique* **64**, No. 10, 817-827.

Clayton, C. R. I., Siddique, A. & Hopper, R. J. (1998). Effects of sampler design on tube sampling disturbance – numerical and analytical investigations. *Géotechnique* **48**, No. 6, 847-867.

Cocjin, M. J., Gourvenec, S. M., White, D. J. & Randolph, M. F. (2014). Tolerably mobile subsea foundations–observations of performance. *Géotechnique* **64**, No. 11, 895-909.

De Catania, S., Breen, J., Gaudin, C. & White, D. J. (2010). Development of multiple-axis actuator control system. *Int. Conf. on Physical Modelling in Geotechnics.* Zurich, Switzerland, 325-330.

Gaudin, C., White, D. J., Boylan, N., Breen, J., Brown, T., De Catania, S. & Hortin, P. (2009). A wireless high-speed data acquisition system for geotechnical centrifuge model testing. *Measurement Science and Technology* **20**, No. 9, 1-11.

Hill, A. J. & Jacob, H. (2008). OTC 19528: In-situ measurement of pipe-soil interaction in deep water. Offshore Technology Conference, 5-8 May 2008, Houston, Texas, USA.

Hover, E. D., Ni, Q. & Guymer, I. (2013). Investigation of centreline strain path during tube penetration using transparent soil and particle image velocimetry. *Géotechnique Letters* **3**, No. 2, 37-41.

Hu, Y. & Randolph, M. F. (1998). A practical numerical approach for large deformation problems in soil. *International Journal of Numerical and Analytical Methods in Geomechanics* **22**, No. 5, 327-350.

Hu, P., Stanier, S. A., Cassidy, M. J. & Wang, D. (2014). Predicting peak resistance of spudcan penetrating sand overlaying clay. *J. Geotech. Geoenviron. Engng ASCE* **140**, No. 2.

Kuo, M.Y., Vincent, C. M., Bolton, M. D., Hill, A. & Rattley, M. (2015). A new torsional shear device for pipeline interface shear testing. *Frontiers in Offshore Geotechnics III – Meyer (Ed.)*, 405-410.

Lee, K. K., Cassidy, M. J. & Randolph, M. F. (2013). Bearing capacity on sand overlying clay soils: experimental and finite-element investigation of potential punch-through failure. *Géotechnique* **63**, No. 15, 1271-1284.

Lehane, B. M. & Liu, Q. B. (2013). Measurement of shearing characteristics of granular materials at low stress levels in a shear box. *Geotechnical and Geological Engineering*, No. 31, 329-336.

Pedersen, R., Olson, R. & Rauch, A. (2003). Shear and interface strength of clay at very low effective stress. *Geotechnical Testing Journal* **26**, No. 1, 71-78.

Randolph, M. F., White, D. J. & Yan, Y. (2012). Modelling the axial resistance on deep water pipelines. *Géotechnique* **62**, No. 9, 837-846.

Randolph, M. F. & Hope, S. (2004). Effect of cone velocity on cone resistance and excess pore pressures. In *Proceedings of Proc., Int. Symp. on Engineering Practice and Performance of Soft Deposits*. Yodagawa Kogisha Co., Ltd., pp. 147-152.

Richardson, M. (2007). Rowe cell test on kaolin clay, COFS internal report. Centre for Offshore Foundation Systems, UWA, Crawley, Western Australia.

Schneider, M. A., Stanier, S. A., Chatterjee, S., White, D. J. & Randolph, M. F. (2018). The parkable piezoprobe for determining c_v and strength – modelling and interpretation methods. *Submitted to Géotechnique*.

Stanier, S. A. & White, D. J. (2014). Shallow penetrometer penetration resistance. *Journal of Geotechnical and Geoenvironmental Engineering* **141**, No. 3, 04014117.

Sully, J. P., Robertson, P. K., Campanella, R. G. & Woeller, D. J. (1999). An approach to evaluation of field CPTU dissipation data in overconsolidated fine-grained soils. *Canadian Geotechnical Journal* **36**, No. 2, 369-381.

Westgate, Z.J., White, D.J. & Randolph, M.F. (2013). Modelling the embedment process during offshore pipe-laying on fine-grained soils. *Canadian Geotechnical Journal* **50**, No. 1, 15-27.

White, D. J. & Randolph, M. F. (2007). Seabed characterisation and models for pipeline-soil interaction. *International Journal of Offshore and Polar Engineering* **17**, No. 3, 193-204.

White, D. J., Gaudin, C., Boylan, N. & Zhou, H. (2010). Interpretation of T-bar penetrometer tests at shallow embedment and in very soft soils. *Canadian Geotechnical Journal* **47**, No. 2, 218-229.

White, D. J., Hill, A. J., Westgate, Z. J. & Ballard, J-C. (2010). Observations of pipe-soil response from the first deep water deployment of the SMARTPIPE. *Frontiers in Offshore Geotechnics II – Gourvenec & White (eds)*, 851-856.

White, D.J., Stanier, S.A., O'Loughlin, C.D., Chow, S.H., Randolph, M.F., Draper, S., Mohr, H., Morton, J., Peuchen, J., Fearon, R., Roux, A. & Chow, F. (2017) Remote intelligent geotechnical seabed surveys - technology emerging from the RIGSS JIP. Offshore Site Investigation and Geotechnics 2017 Conference Proceedings: Proceedings of the 8th International Conference. Society for Underwater Technology. 9 pp.

Yan, Y., White, D. J. & Randolph, M. F. (2011). Penetration resistance and stiffness factors for hemispherical and toroidal penetrometers in uniform clay. *International Journal of Geomechanics* **11**, No. 4, 263-275.

Yan, Y., White, D. J. & Randolph, M. F. (2014). Cyclic consolidation and axial friction for seabed pipelines. *Géotechnique Letters*, No. 4, 165-169.

Yan, Y., White, D. J. & Randolph, M. F. (2017). Elastoplastic consolidation solutions for scaling from shallow penetrometers to pipelines. *Canadian Geotechnical Journal* **54**, No. 6, 881-895.

Yan, Y. (2014). Novel methods for characterising pipe-soil interaction forces in-situ in deep water. PhD thesis submitted to the University of Western Australia.

FIGURES

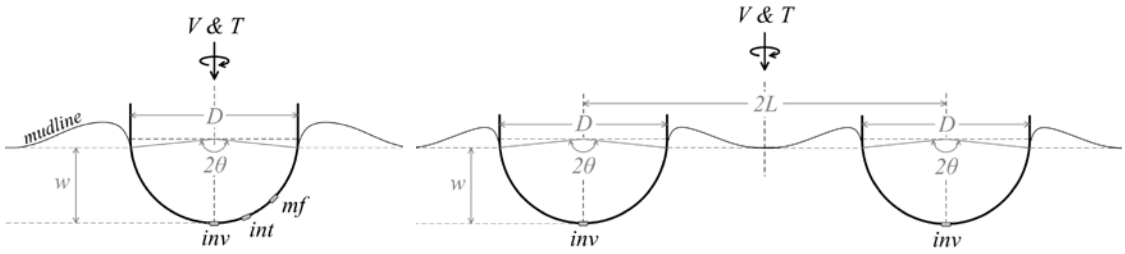

(a) (b)

Figure 1: Schematic illustration and used nomenclature: (a) hemiball; and (b) toroid with pore pressure transducers positioned on the invert (inv), intermediate (int) and midface locations (mf).

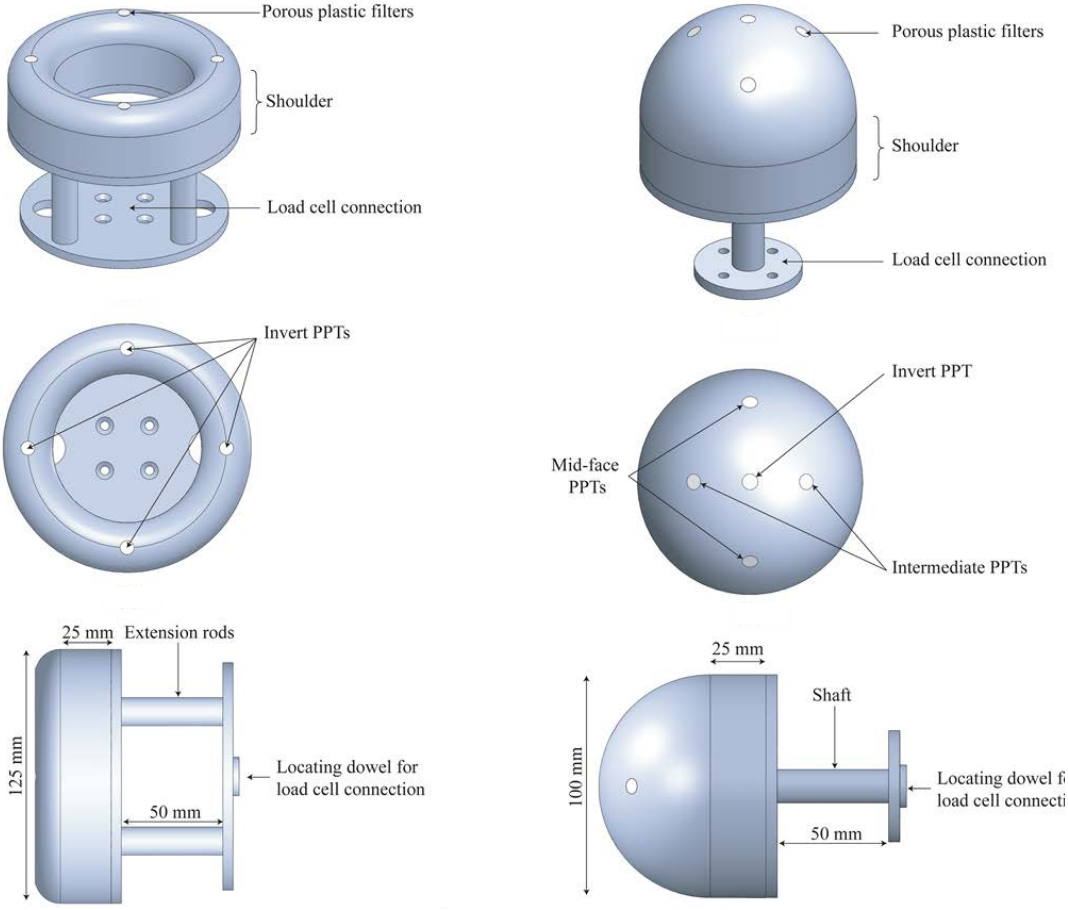

(a) (b)

Figure 2: Rendered drawings of: (a) toroid; and (b) hemiball penetrometer.

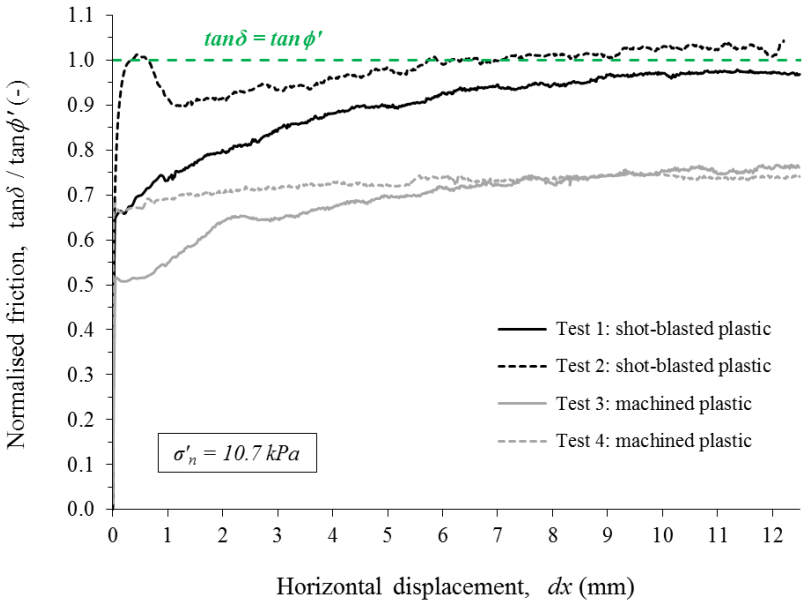

Figure 3: Typical interface shear box test to determine the proportion of friction mobilised by the shallow penetrometer interface.

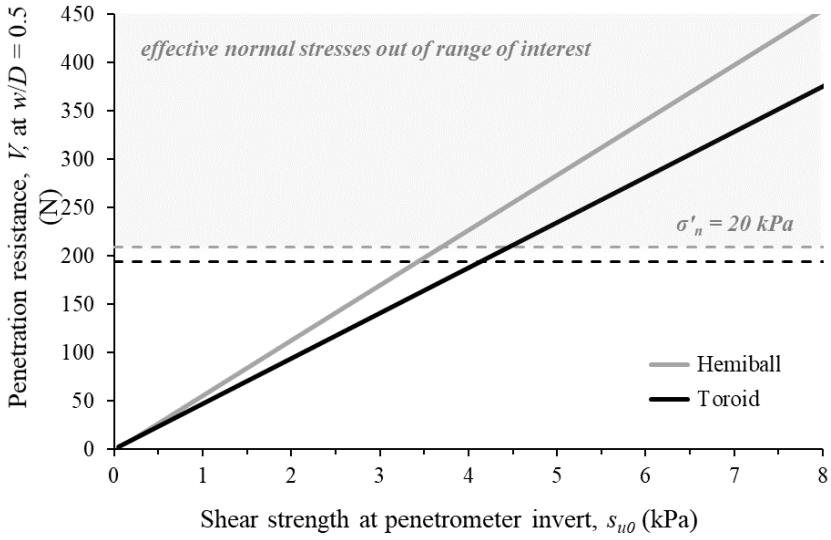

(a)

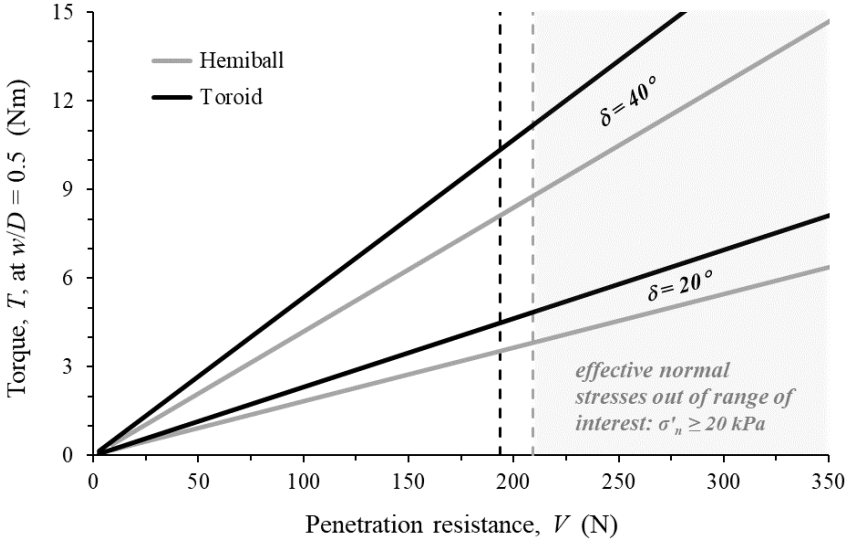

(b)

Figure 4: Dimensioning of the load cell: (a) required capacity for penetration resistance (vertical force); and (b) required torsional capacity (torque) for the box-core hemiball (D = 100 mm) and toroid (D = 25 mm) penetrometer.

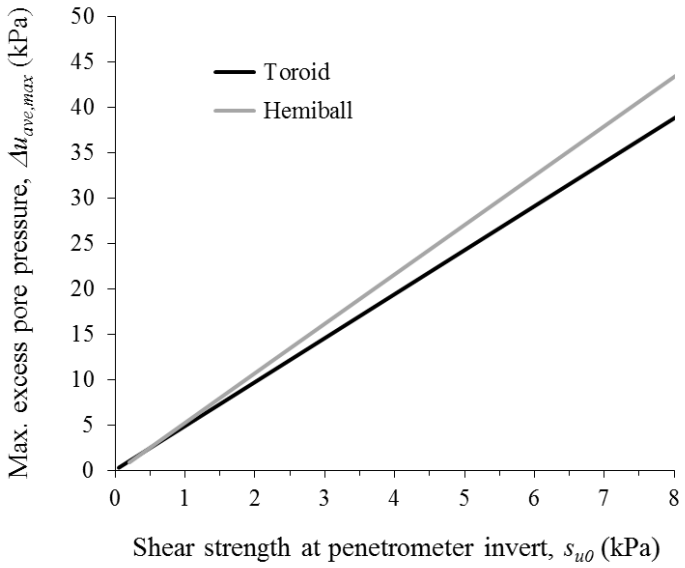

Figure 5: Expected excess pore water pressures generated during initial undrained penetration to a depth of $w/D = 0.5$.

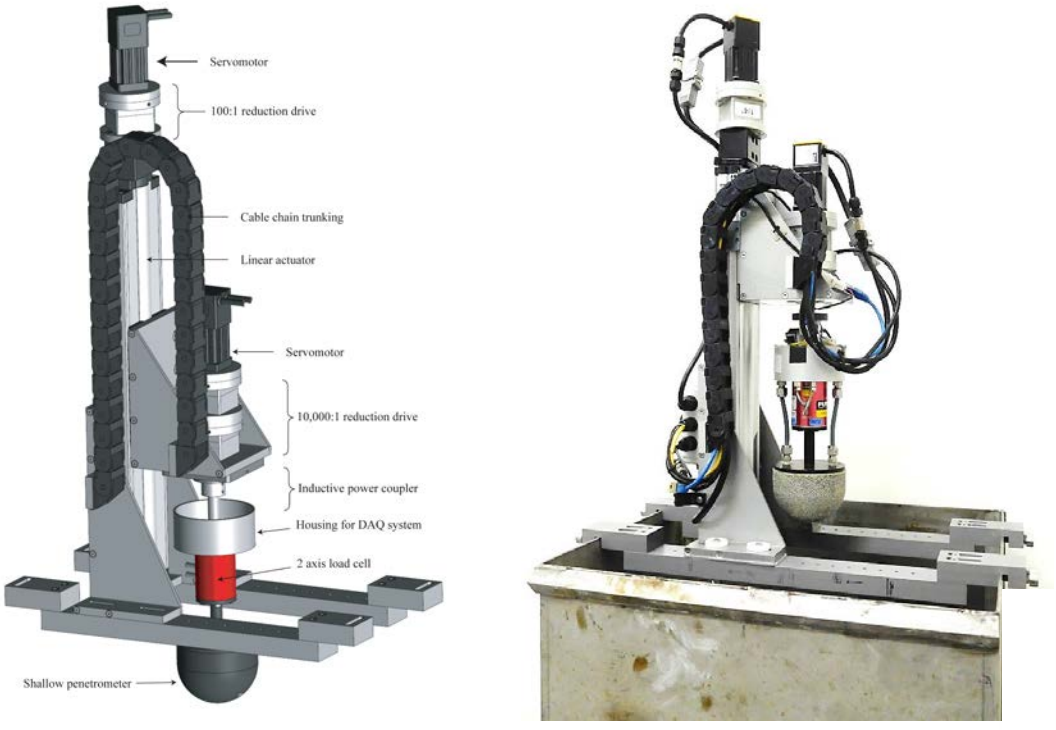

(a) (b)

Figure 6: Recommended design of box core actuator: (a) detailed engineering drawing with crossbars for laboratory use; and (b) picture of fabricated system mounted to a box core sleeve.

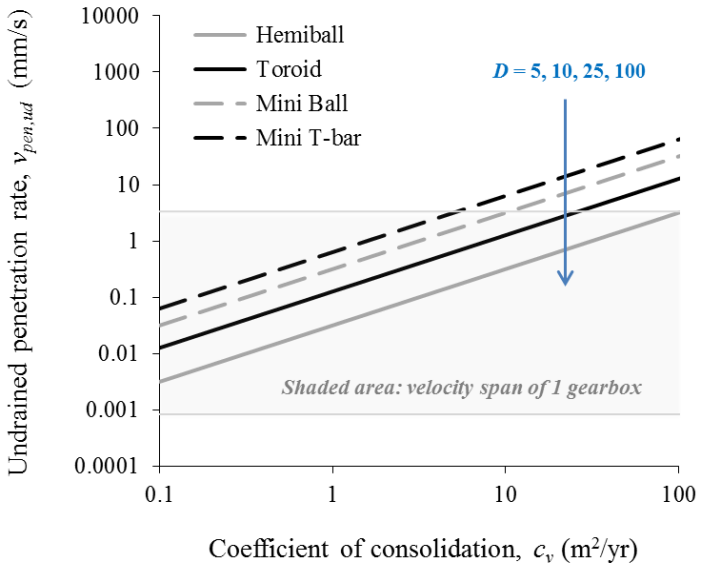

(a)

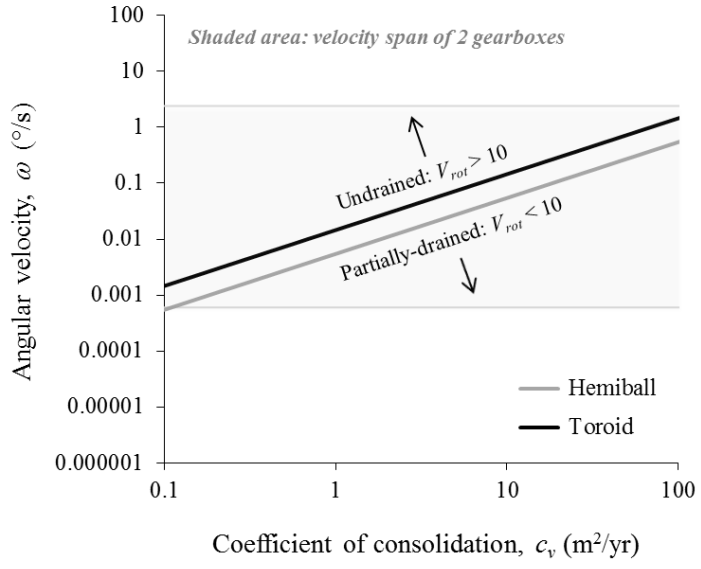

(b)

Figure 7: Drive speed requirements for (a) vertical axis; and (b) rotational axis.

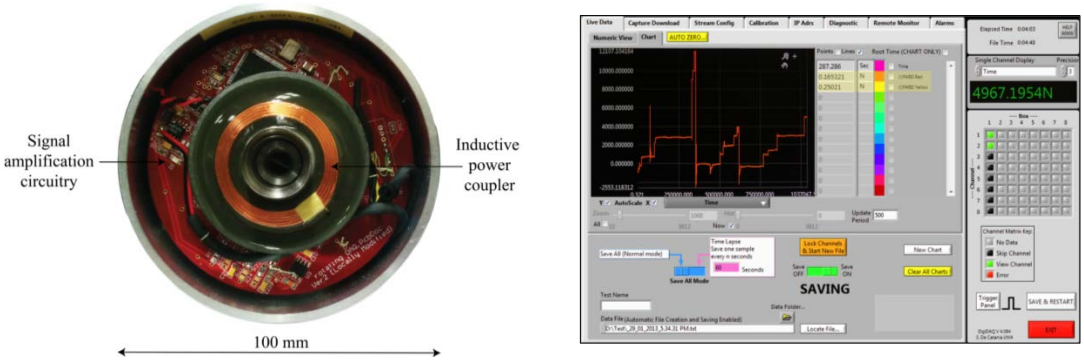

(a) *(b)*

Figure 8: (a) Custom-built wireless DAQ system; and (b) DigiDAQ software for data logging.

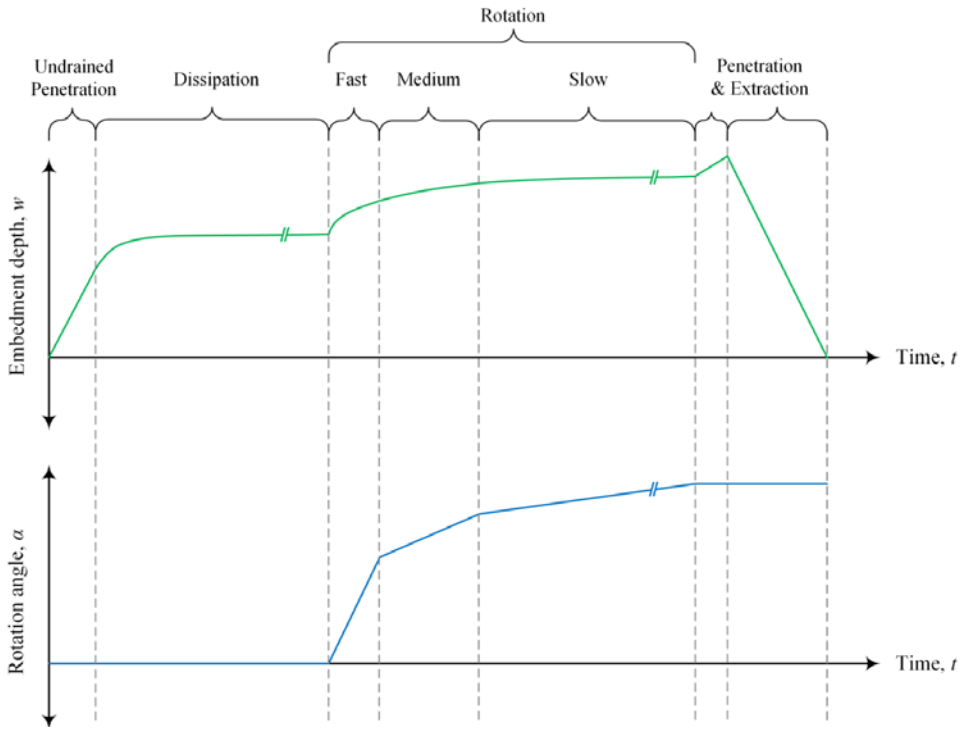

Figure 9: Testing stages of a basic shallow penetrometer test (displacement and rotation).

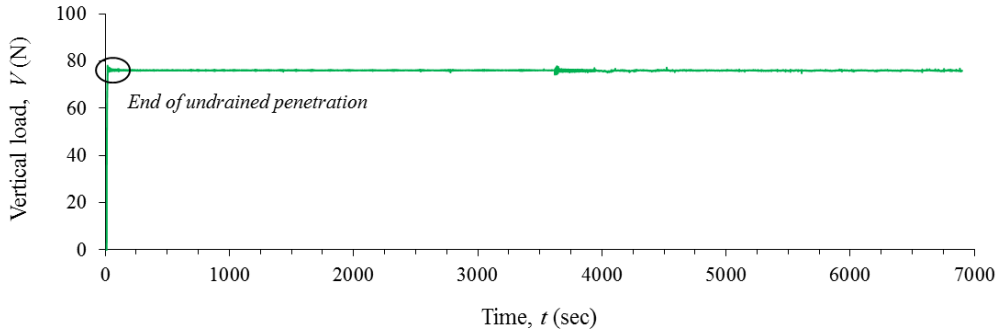

(a)

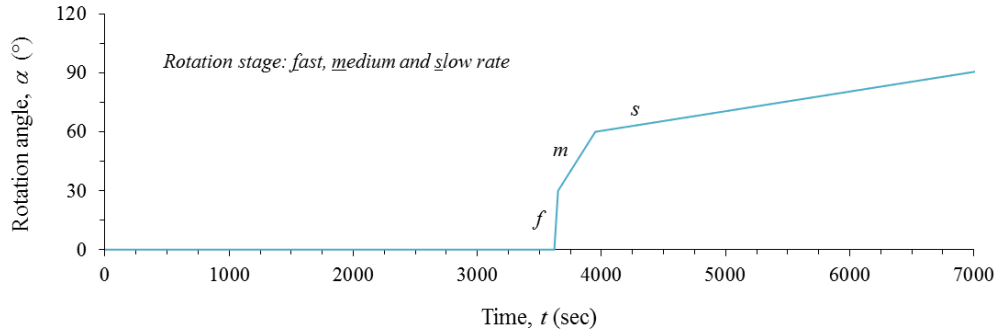

(b)

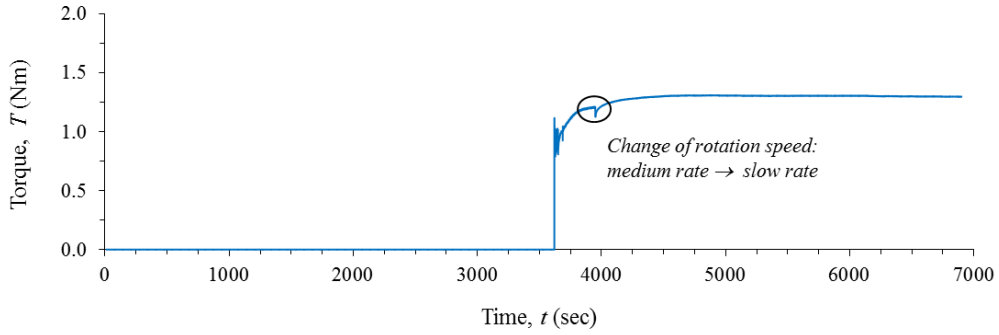

(c)

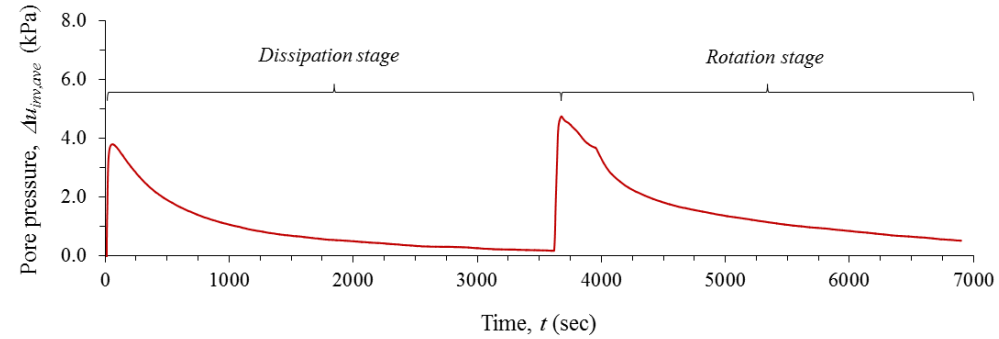

(d)

Figure 10: Time histories for an example toroid test: (a) the applied vertical load; (b) the recorded rotation angle; (c) the measured torque; and (d) average excess pore water pressure.

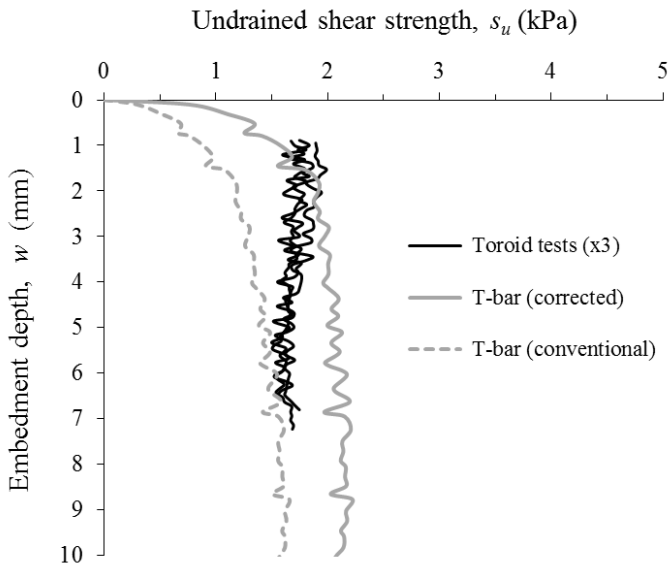

Figure 11: Back-analysis of penetration stage: toroid vs. T-bar

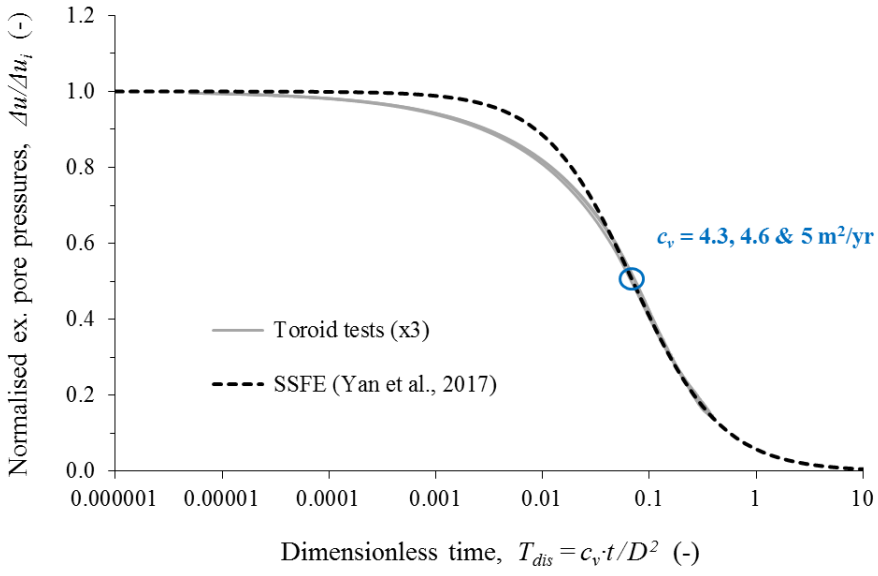

(a)

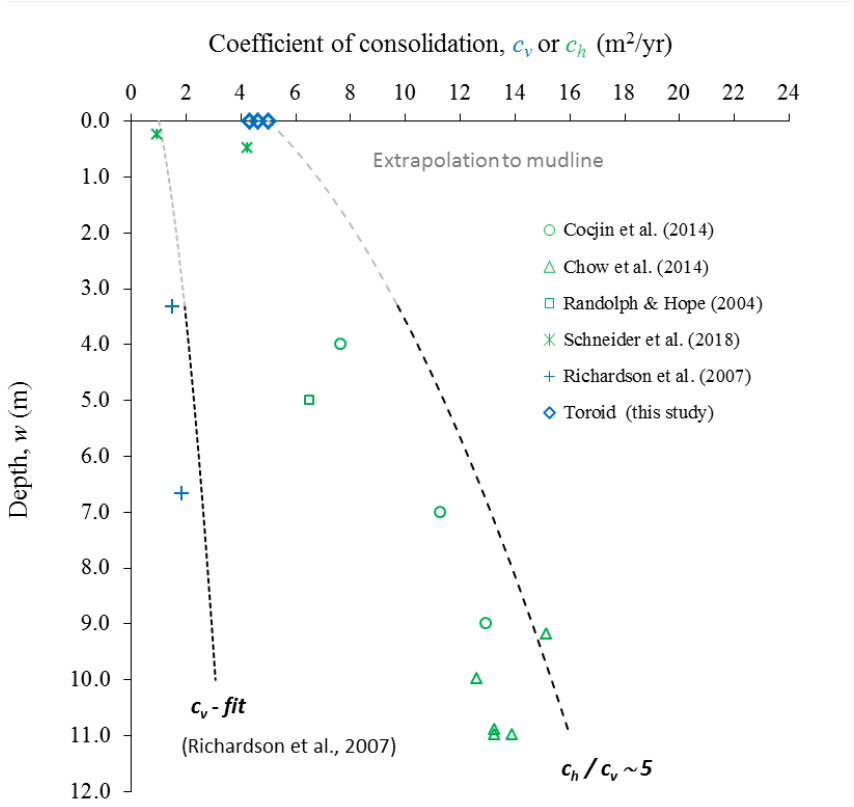

(b)

Figure 12: Dissipation stage: (a) dimensionless time vs. normalised excess pore pressure; and (b) comparison of inferred coefficients of consolidation to existing literature for kaolin clay.

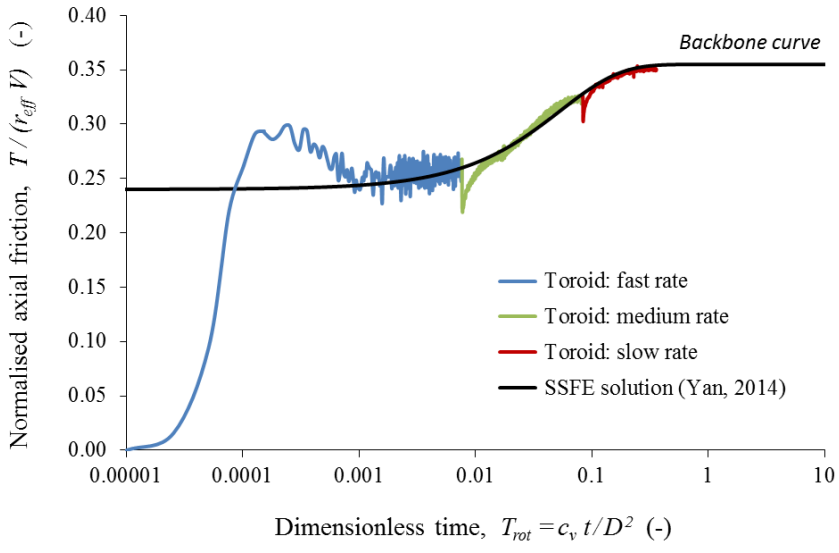

(a)

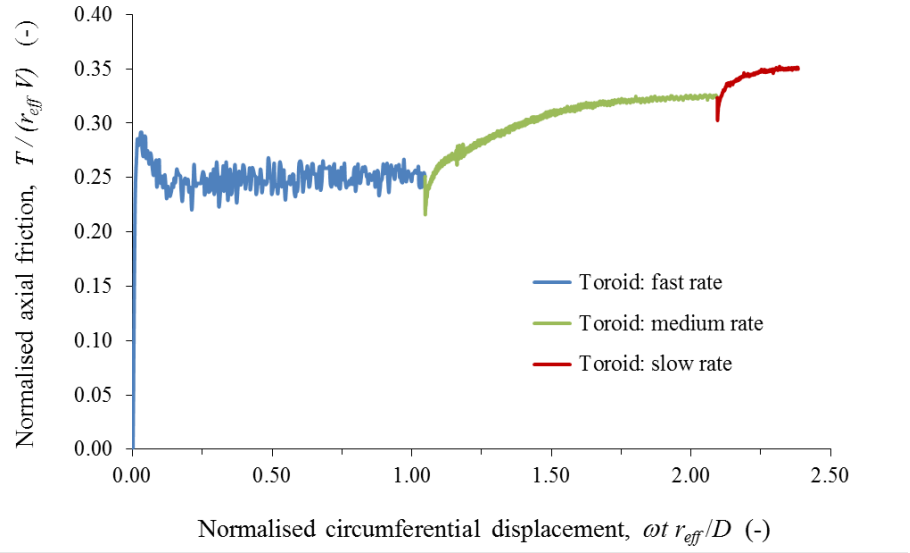

(b)

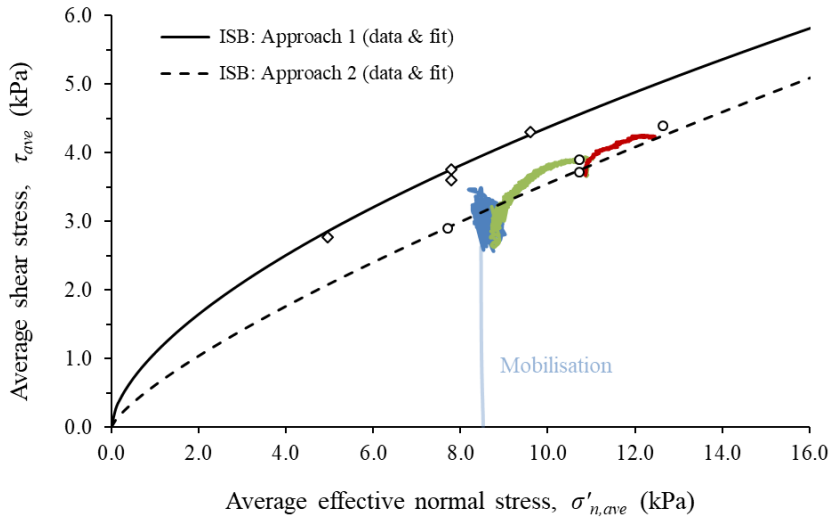

(c)

Figure 13: Back-analysis of rotation stage: (a) dimensionless time vs. normalised axial friction; (b) dimensionless displacement vs. normalised axial friction; and (c) effective stress interpretation.